Propane selective carbon adsorbents from phenolic resin precursor

Márcia Andrade [a], Andrew J. Parnell [b], Gabriel Bernardo [a], Adélio Mendes [a],[*]

[a] *LEPABE – Laboratory for Process Engineering, Environment, Biotechnology and Energy, Faculty of Engineering University of Porto, Portugal*
[b] *Department of Physics and Astronomy, University of Sheffield, S3 7RH, UK*

A B S T R A C T

Novel carbon adsorbents for propane/propylene separation, with an unprecedented adsorption selectivity to propane – the minority component – were prepared from a phenolic resin precursor. The preparation conditions of the carbon molecular sieve adsorbents, such as pre-treatment with phosphoric acid, carbonization and post-treatment with propylene, were carefully investigated concerning their role on the separation performance. The best performing sample, MFF_8, was characterized by SEM, FTIR and small-angle X-ray scattering (SAXS). It was concluded that the pre-treatment with phosphoric acid was critical for obtaining the propane/propylene separation performance – adsorption ratio of *ca.* 2 at 1 bar and 25 °C; this sample was carbonized at 1100 °C and post-treated with propylene during 12 days. SAXS analysis indicates rod-shaped pores for the MFF_8 sample with a bimodal size distribution with averages of 0.4 nm and 3.7 nm, and HRTEM images show a network of earthworm micropores. The adsorption selectivity of this adsorbent to propane was assigned to the shape and size of the pores and the rigidity of propylene compared with propane for worming through the constriction of the ultra-micropores network. To the best knowledge of the authors, this is the first time a carbon molecular sieve (CMS) adsorbent with rod-shaped pores is reported. This new family of CMS adsorbents show great potential for equilibrium and kinetic based separations of adsorbates displaying different worming performances.

1. Introduction

Olefins are the building blocks for a large number of commodities [1, 2]. Their separation/purification remains, however, a great challenge. Light olefins such as ethylene and propylene are often mixed with their homologue light paraffins, ethane and propane, respectively, which display close boiling points [2]. One of the most important uses of ethylene and propylene are the production of their corresponding polymers; the required purity for this application is >99.5%, which is quite demanding to reach [3,4]. Since distillation is still the election process for these separations, the corresponding distillation columns need to be very long rendering these separations energy demanding [5, 6]. Literature reports several processes for light olefins production and separation, such as i) adsorption-based processes: temperature swing adsorption (TSA) [7] and pressure swing adsorption (PSA) [2,8,9]; ii) membrane processes: gas permeation [10–12] and pervaporation [13]; iii) reaction processes: catalytic pyrolysis process (CPP) [14], by-product upgrading (C4-9) [15] and propane oxidative dehydrogenation [16]; and iv) hybrid processes: distillation with adsorption [17], membrane [18] and reaction processes [19]. Among the above processes,

adsorption- [20] and membrane-based [21] are the ones that have received more attention. Especially, adsorption-based processes have reached promising recoveries for the required purities [2,8].

Rege et al. [20] studied the performance of an equilibrium PSA-based separation adsorbent, $AgNO_3/SiO_2$, and a kinetic separation adsorbent, zeolite 4A. Comparing the performance of both adsorbent materials, the authors found that $AgNO_3/SiO_2$ displayed a better separation performance allowing to produce a propylene 99% with a recovery of 44%. Padin et al. [22] simulated the performance of an $AlPO_4$-14 adsorbent using a four-step PSA cycle with a gas feed of 50% C_3H_6/50% C_3H_8. The results showed a propylene purity of 99% and a recovery of 53%. Grande et al. [2] used a zeolite 4A adsorbent in a two-stage VPSA unit, obtaining a propylene purity of 99.6% and a recovery of 95.9%. Despite the very satisfactory results, the energy demand of the overall separation was somewhat higher than the one for distillation process. Furthermore, Campo et al. [8] used a modified 13X zeolite in a five-step VPSA and a feed mixture of 75% C_3H_6/25% C_3H_8. The obtained results showed a propylene purity of 99.54% and a recovery of 85%, which are very interesting results. Although the reported results display the required propylene purity, *ca.* 99.0 %–99.5%, the recovery is still relatively low,

---

ca. 50.0–85.0% [2]. Other studies have assessed the adsorption and kinetic selectivity of propylene/propane mixtures in: zeolite 13X pellets [23]; zeolite DD3R with different sizes [24]; zeolite 5A with deposited ultrathin microporous TiO_2 coatings to precisely adjust the pore mouth size [25]; ferro-alumino-silicate levyne (FeAl-LEV) zeolites [26]; zeolite membranes, containing ion-exchanged silver cations [27]; Ag(I) doped microporous carbons [28]. However, all the adsorbents used in these separations are adsorption selective to the olefins, which is the majority component. This makes the PSA units large, energy demanding and displaying modest recoveries.

The ideal would be to have an adsorbent selective to the minority component, the light paraffin. However, there were described just a handful of such adsorbents. Herdes et al. [29] were among the first to report a paraffin equilibrium selective absorbent. These authors described an aluminium methylphosphonate polymorph alpha (AlMePO-α) selective towards paraffins over olefins. This material – $Al_2(PO_3CH_3)_3$ – was firstly reported by Maeda et al. [30] and since then it was widely studied by other researchers [31–33]. Literature assign this inversed selectivity to strong adsorbent-adsorbate interactions during adsorption process [34–36]. Additionally, metal organic frameworks (MOFs) such as ZIF-7, $Fe_2(O_2)(dobdc)$ and MIL-100 have been investigated for preferable paraffin selectivity over olefins i) ethane/ethylene [5], ii) propane/propylene [37,38] and iii) isobutane/isobutene [38] separations. Gücüyener et al. [5] reported a MOF, ZIF-7, paraffin selective towards ethane/ethylene mixtures displaying an adsorbed concentration ratio of *ca.* 7, favourable to ethane over ethene, with an ethane adsorption capacity of 1.8 mol·kg^{-1}, at 0.3 bar 25 °C. Recently, Andres-Garcia et al. [39] reported a ZIF-67 MOF that exhibited an adsorbed concentration ratio, favourable to propane over propylene, of 3.7 with a propane adsorption capacity of 2.24 mol·kg^{-1}, at *ca.* 0.2 bar and 25 °C.

The discovery of new materials selective towards paraffins over olefins may require changing the structure of the adsorbents, such as functional surface groups and/or pore structure [36]. Finding the key factors for having the unprecedented separation would allow the development and optimization of materials with the desired characteristics for the given gas separation. Some authors are developing different concepts for explaining this separation such as thermodynamic control, *i.e.*, control of specific adsorbate-adsorbent interactions [40]. Studies revealed that whereas polar cation-containing zeolites, such as 13X, show preferable olefin adsorption [41,42], nonpolar cation-free zeolites display higher affinity to paraffins [36,43,44]. These studies of preferable paraffin adsorption were predicted based on molecular dynamics calculations using mixed gas isotherms [40]. For example, Keil et al. [45] predicted an ethane adsorbed capacity selectivity of 2 from an equimolar mixture of ethane/ethene with an ethane adsorption capacity of 2.5 mol·kg^{-1} on carbon nanotubes, at 1 bar and 27 °C. On the other hand, it was predicted that zeolite silicalite-1 should display only a slightly higher ethane adsorption equilibrium over ethylene [46].

This work reports the preparation of propane selective carbon molecular sieve adsorbents from a phenolic resin precursor. The samples were pre-treated with phosphoric acid and post-treated with propylene; propylene treatment stabilizes the adsorbent against chemisorption of ambient oxygen [47–49]. Adsorbents were characterized concerning adsorption equilibrium isotherms of propane and propylene, pore size distribution and mercury porosimetry; the surface morphology and chemistry were analysed by scanning electron microscopy (SEM), Fourier transform infrared spectroscopy (FTIR) and by thermogravimetric analysis; the pore shape and pore size distribution was obtained by SAXS. The best performing material displayed a propane/propylene adsorbed concentration ratio of *ca.* 2 at 1 bar.

2. Experimental

2.1. CMS preparation

2.1.1. Precursor materials

Phenolic resin MFF, mean particle size of *ca.* 1.5 μm, was used as precursor. Carbon dioxide (99.9% pure) and helium (99.999% pure) were supplied by Linde. Propane and propylene were provided from Praxair (99.5% pure).

2.1.2. Pre-treatments

MFF precursor was mixed overnight with 0–25 wt % phosphoric acid solution at room temperature; the acid:precursor mass ratio was *ca.* 3. After mixed, the samples were carbonized.

2.1.3. Carbonization

The carbonization step was carried out in an alumina tube (one of 954 cm^3 volume for temperatures among 950–1100 °C and another of 5049 cm^3 volume for temperatures between 1200 and 1300 °C; with 4.7 cm and 7.1 cm of inner diameter, respectively) inside a tubular horizontal Termolab TH furnace. For guaranteeing the temperature homogeneity along the tube, three spatially separated thermocouples were placed into the furnace. Samples were carbonized under N_2 atmosphere with a 100 mL·min^{-1} (small volume tube) and 300 mL·min^{-1} (large volume tube) flow rate and a 3 °C·min^{-1} heating rate. End temperatures from 950 °C up to 1300 °C with 60 min of soaking time were employed [50]. After the carbonization, the carbon adsorbents were cooled naturally until room temperature and then removed from the furnace.

2.1.4. Post-treatments

After the carbonization step, the carbon adsorbents were stored in 2 bar of propylene for 1–12 days.

2.2. Thermogravimetric analysis

Thermogravimetric analysis was performed in a Netzsch STA 449 F3 Jupiter thermogravimetric balance; a sample of 11.1 mg was employed. A proximate analysis was performed for obtaining the fraction of fixed carbon. The protocol used is described elsewhere [51] and generally comprises the following steps:

- From room temperature to 110 °C at 25 °C·min^{-1} under 30 mL min^{-1} of nitrogen; in this step all humidity should be released.
- From 110 °C up to 950 °C under nitrogen stream; in this step it is expected a mass loss attributed to the release of volatile matter.
- The last step at 950 °C includes a 9 min dwell under nitrogen and a 11 min dwell under oxygen atmosphere, where carbon was burned leaving ashes.

2.3. Scanning electron microscopy (SEM)

SEM analyses were performed in a Phenom XL scanning electron microscope. The Phenom XL was equipped with two detector systems, one with a fully integrated EDS system for elemental analysis and another that corresponds to a Secondary Electron Detector (SED) that enables surface sensitive imaging.

2.4. Mercury porosimetry

Mercury porosimetry analysis was performed in a Micromeritics Autopore IV 9500 porosimeter. Samples were mechanically outgassed while under 3.45×10^{-3} MPa prior to mercury intrusion for removing all physically adsorbed species. Mercury pressure increased from 3.45×10^{-3} MPa to 2.068×10^2 MPa for entering in smaller pores, down to *ca.* 6 nm.

Table 1
Adsorbents preparation conditions description.

Sample	Pre-treatment	Carbonization end temp.	Post-treatment
MFF_1	Without	1100 °C for 1 h	Without
MFF_2	25 wt% of H_3PO_4 overnight	1100 °C for 1 h	Without
MFF_3	Without	1100 °C for 1 h	Propylene for 1 day
MFF_4	Without	1100 °C for 1 h	Propylene for 7 days
MFF_5	12.5 wt% of H_3PO_4 overnight	1100 °C for 1 h	Propylene for 12 days
MFF_6	25 wt% of H_3PO_4 overnight	950 °C for 1 h	Propylene for 12 days
MFF_7	25 wt% of H_3PO_4 overnight	1100 °C for 1 h	Propylene for 6 days
MFF_8	25 wt% of H_3PO_4 overnight	1100 °C for 1 h	Propylene for 12 days
MFF_8/ 1200	25 wt% of H_3PO_4 overnight	1200 °C for 1 h	Propylene for 12 days
MFF_8/ 1300	25 wt% of H_3PO_4 overnight	1300 °C for 1 h	Propylene for 12 days

Table 2
Adsorption capacity and kinetics for both C_3H_8 and C_3H_6 and at *ca.* 1 bar and 25 °C.

Sample	C_3H_8		C_3H_6		C_3H_8 selectivity	
	$q/$ $mol \cdot kg^{-1}$	$D \cdot r^{-2}/$ s^{-1}	$q/$ $mol \cdot kg^{-1}$	$D \cdot r^{-2}/$ s^{-1}	Equil.*	Kinet.*
MFF_1	0.4	1.9×10^{-3}	1.6	1.2×10^{-3}	<1	1.6
MFF_2	3.0	1.9×10^{-3}	2.5	2.5×10^{-3}	1.2	≈ 1
MFF_3	0.2	1.2×10^{-2}	1.8	3.3×10^{-4}	<1	37.1
MFF_4	0.3	4.0×10^{-2}	1.6	7.3×10^{-3}	<1	5.5
MFF_5	2.0	3.9×10^{-2}	2.3	2.4×10^{-2}	<1	1.6
MFF_6	2.4	5.0×10^{-2}	2.9	4.5×10^{-2}	<1	1.1
MFF_7	2.7	3.1×10^{-2}	2.5	1.5×10^{-3}	1.1	21.2
MFF_8	2.9	1.2×10^{-1}	1.4	1.4×10^{-1}	2.1	≈ 1
MFF_8/ 1200	3.7	1.8×10^{-1}	3.5	3.9×10^{-2}	1.1	4.7
MFF_8/ 1300	3.8	2.4×10^{-2}	3.3	4.2×10^{-2}	1.2	<1

2.5. Particle size distribution

Particle size measurements were performed using a Counter LS 230 using Mie light scattering Polarization Intensity Differential Scattering (PIDS) technology. Samples were previously dispersed in distilled water.

2.6. Fourier transform infrared spectroscopy (FTIR)

The infrared spectra were recorded using a VERTEX 70 FTIR spectrometer (BRUKER) in transmittance mode with a high sensitivity DLaTGS detector at room temperature. Samples were analysed in transmission mode, using pellets of potassium bromide (KBr) with 1% (w/w) of the compound. The spectra were recorded from 4000 cm^{-1} to 400 cm^{-1} with a resolution of 4 cm^{-1}.

2.7. Micropores characterization

Micropore size distribution of the CMS adsorbents was determined based on adsorption equilibrium isotherms of carbon dioxide at 0 °C as
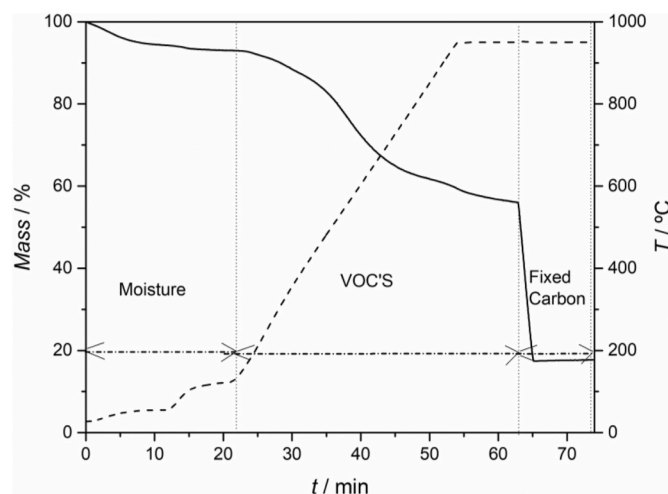

Fig. 1. Proximate analysis of MFF precursor by thermogravimetric method. The removed species at different intervals are identified.

described elsewhere [52–54]. This method could not be applied to phosphoric acid treated samples due to the change of the CMS inner surface chemistry.

For characterizing the adsorbent microporosity the Dubinin-Astakhov (DA) equation is normally used (Eq. (1)) [55,56]:

$$\frac{W}{W_0} = \exp\left[-\left(\frac{RT \ln(P_0/P)}{E_0}\right)^n \right] \tag{1}$$

where W is the micropore volume, P is the pressure, W_0 is the total micropore volume, E_0 is the characteristic energy for adsorption, P_0 is the vapor pressure of the free liquid, R is the gas constant, T is the absolute temperature and n is a fitting parameter; for $n = 2$ this equation renders the Dubinin–Raduschkevisch (DR) equation.

2.8. Small-angle X-ray scattering

SAXS measurements were carried out at the University of Sheffield using a Xeuss 2.0 instrument (Xenocs, Grenoble France), this particular SAXS system is equipped with a liquid gallium X-ray source (MetalJet Excillum, Sweden). The X-ray beam (9.24 keV) size was 600 μm vertically and 400 μm horizontally, with a distance of 305 mm between sample position and the detector (Pilatus3R 1 M 2D, Dectris, Switzerland). The samples were mounted on a sample holder and three measurements were taken from different regions of the sample, spaced by roughly ~1 mm. Each sample was also measured in transmission and scaled to the transmission through air and a suitable air background was also collected. The data operation tool in Sasview 4.2 [57] was used to scale the SAXS data and subtract the air background.

2.9. High-resolution transmission electron microscopy (HRTEM)

HRTEM analysis was performed in a FEI Titan Cubed microscope operated at 300 kV. This instrument was equipped with an image aberration corrector that provides 80 pm resolution.

Table 3
Proximate analysis results by thermogravimetry of MFF precursor.

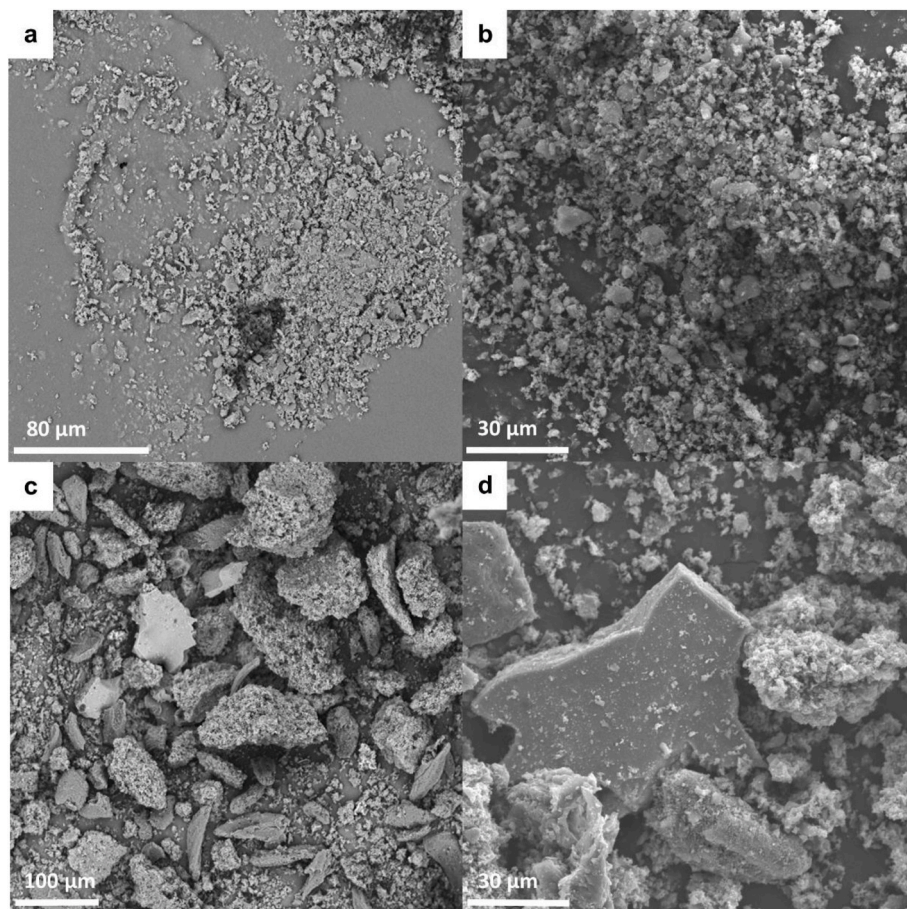|	MFF.AP precursor
Humidity/%	7
Volatile matter/%	34
Fixed carbon/%	41
Ashes/%	18

Fig. 2. SEM micrographs with a) 1000 × b) 2000 × of magnification for MFF precursor material and c) 500 × d) 2000 × of magnification for the MFF_8 CMS adsorbent.

2.10. Specific surface area

Multipoint Brunauer-Emmett-Teller (BET) specific surface area measurements were performed in a Quantachrome Autosorb AS-1 instrument at −196 °C. Prior to the analysis samples were outgassed at 80 °C for 30 min, then at 120 °C for 30 min and finally at 300 °C for 3 h.

2.11. Adsorption equilibrium isotherms and gas uptake experiments

The adsorption equilibrium isotherms and uptake curves for C_3H_6, C_3H_8 and CO_2 were obtained by using the volumetric method as described elsewhere [58,59]. For measuring pressures until 2 bar a 2 bar Drück pressure sensor was used (reading error of 0.1% of full scale), and for higher pressure values a 7 bar Drück (reading error of 0.1% of full scale) was employed. The samples and tanks were evacuated at 70 °C for 4 h to pressures <0.002 bar using an Alcatel 1004A vacuum pump.

Langmuir (Eq. (2)) and Toth (Eq. (3)) adsorption isotherm equations are thermodynamically consistent; Toth has one more parameter to account for the surface heterogeneities [56]. SIPS (Eq. (4)) also has three parameters to account for the surface heterogeneities but is not applicable for low pressures since it does not converge to the Henry's law [54, 56].

$$q = q_s \frac{bP}{1 + bP} \tag{2}$$

$$q = q_s \frac{bP}{\left(1 + (bP)^t\right)^{1/t}} \tag{3}$$
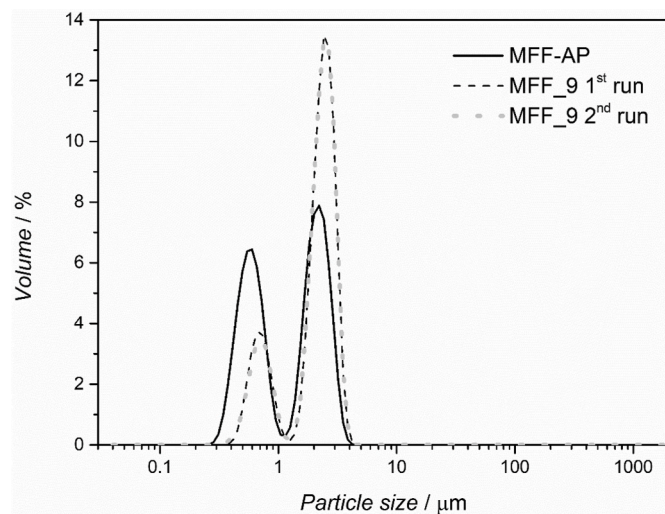

Fig. 3. Particle size distribution of precursor MFF and of the derived CMS adsorbent MFF_8.

$$q = q_s \frac{(bP)^{1/n}}{1 + (bP)^{1/n}} \tag{4}$$

where q is the adsorbed solute concentration at pressure P, q_s is the adsorbed saturation capacity, b the adsorption affinity constant and t and n are parameters used to characterize the heterogeneity of the
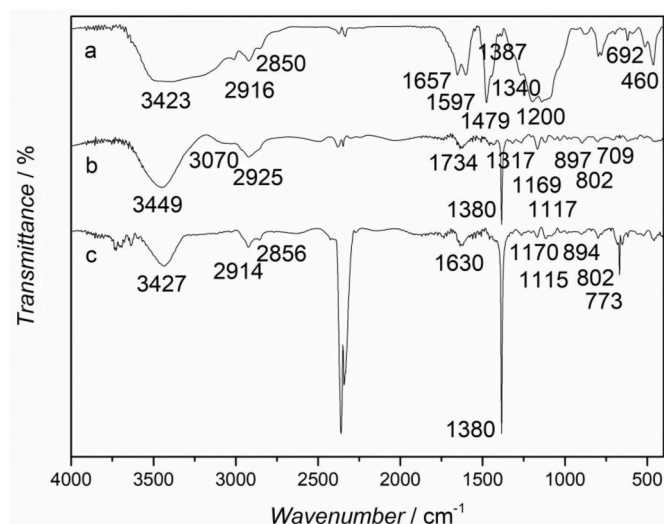
Fig. 4. FTIR spectrum: a) precursor (sample MFF) and; b) sample MFF_2, pre-treated with phosphoric acid and without post-treatment; c) sample MFF_8, pre-treated with phosphoric acid and post-treated with propylene for 12 days.

system. Generally, t is less than unity; for $t = 1$, Toth equation converges to Langmuir equation [56].

The adsorption kinetics was calculated using a non-isothermal model for constant-volume and variable-pressure conditions (Eq. (5)) [60]:

$$F = 1 - \sum_{n=1}^{\infty} \frac{9(1+\alpha^*)\left[\frac{Y_n}{-q_n^2}\right]^2 \exp\left(-q_n^2\tau\right)}{\frac{1}{\beta_n^2} + \frac{3}{2}\frac{\beta}{\beta_n^2}\left[q_n \cot q_n\left(\frac{Y_n}{q_n^2}\right) + 1\right] + \frac{3}{2}\frac{\alpha^* B_n}{q_n^4 \beta_n}} \tag{5}$$

where $B_n = Y_n \left[(q_n^2 - \alpha)\, q_n \cot q_n - 2\alpha\right] + q_n^2(q_n^2 - \alpha)$, $Y_n = q_n \cot q_n - 1$ and $\alpha^* = KV$. Considering that $V = V_s/V_g$, and V_S correspond to the volume of the sorbent particles and V_g to the volume of the gaseous phase, respectively. This equation was fitted to the experimental uptake curves for obtaining the inverse of the apparent diffusion time constant ($D \cdot r^{-2}$).

3. Results and discussions

Several CMS samples were prepared under different conditions – Table 1 – and characterized for optimization of the adsorbent performance; the phosphoric acid pre-treatment, the carbonization end temperature and the post-treatment with propylene were changed.

3.1. CMS adsorption capacity and kinetics

Table 2 shows the obtained propane and propylene adsorbed concentration and $D \cdot r^{-2}$ at *ca.* 1 bar and 25 °C for all samples.

From Table 2 it can be observed that the sample without any pre- or post-treatment – MFF_1 (control) – is selective towards propylene. The propane adsorption selective samples are MFF_2, MFF_7, MFF_8 and MFF_8/1200; MFF_8 sample displays the highest adsorbed concentration ratio of *ca.* 2 at 1 bar. Among these samples MFF_7 and MFF_8/1200 display kinetic selectivity to propane, where sample MFF_7 displays the highest kinetic selectivity of *ca.* 21.

Samples MFF_2 and MFF_8 display the highest equilibrium selectivity and are produced under similar carbonization conditions and pre-treatment; however, sample MFF_8 was also submitted to 12 days of propylene atmosphere treatment. It seems that carbonization conditions and pre-treatment are more relevant than the post-treatment for the adsorption selectivity. MFF_8 displays the highest equilibrium selectivity but also very high adsorption kinetics making it ideal for equilibrium-based PSA gas separation.

Table 4
Mercury porosimetry results for MFF_8 adsorbent.

	MFF_8
$\rho_{He}/g \cdot cm^{-3}$	2.4
Total pore area/$m^2 \cdot g^{-1}$	25.3
Median pore diameter (volume)/μm	0.86
Median pore diameter (area)/μm	0.04
$\varepsilon_{total}/\%$	66.3

3.2. Thermogravimetry analysis

Proximate analysis [51] of precursor MFF was obtained - Fig. 1. Table 3 shows the obtained TGA weight results for MFF precursor.

Proximate analysis shows that the obtained fixed carbon value is within the values for similar materials 40%–60% [61–63]. The fixed carbon is related to the mechanical resistance of the carbonized adsorbent and values above 40% are envisioned [54].

3.3. Scanning electron microscopy

Fig. 2 shows SEM micrographs of MFF precursor material as well as CMS MFF_8.

Fig. 2a) and b) show that the MFF precursor is a very fine powder showing some particle agglomeration. Fig. 2c) and d) show that the resultant CMS adsorbent exhibits larger agglomerated particles. The particle size distribution of sample MFF_8 is shown in Fig. 3; particles range from 0.38 μm to 4 μm.

3.4. Mercury porosimetry

Table 4 summarizes the morphology characteristics of MFF_8 adsorbent, including skeleton density, ρ_{He}, obtained by helium pycnometry.

3.5. FTIR analysis

Fig. 4 shows the FTIR spectra of precursor MFF and samples MFF_2 (pre-treated with phosphoric acid and without post-treatment) and

Table 5
FTIR spectra bands and assignments.

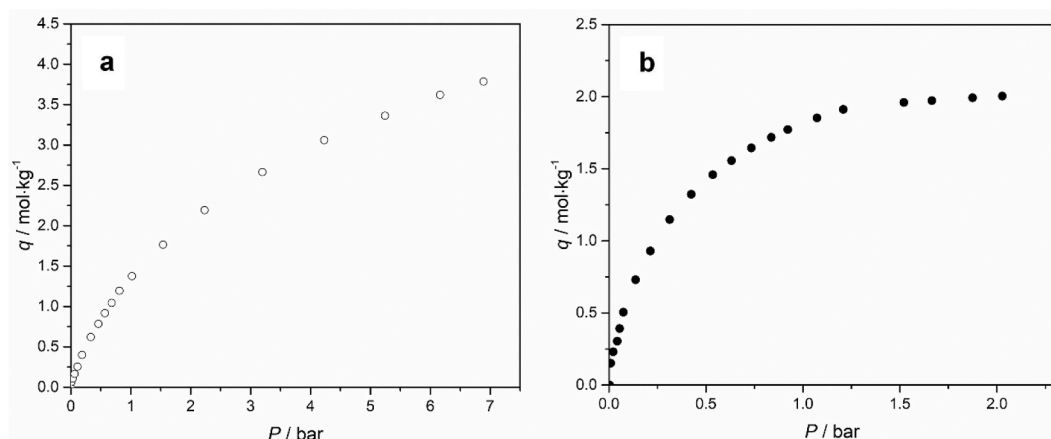| Wavenumber/ cm^{-1}	Functional group	Assignment
3449, 3427, 3423	O–H	O–H stretching assigned to alcohols and phenols
3070	=C–H	=C–H stretching in aromatic structures
2925, 2916, 2914	-CH$_3$ and –CH$_2$-	Aliphatic C–H stretching vibration
2856, 2850	-CH$_2$-	C–H out-of-plane stretching vibration in alkanes
1734	C=O	C=O stretching vibration in ketones, aldehydes, lactones or carboxyl groups
1657, 1597	C=O and NH$_2$	Two bands; C=O stretching and NH$_2$ deformation vibrations
1630	C=C	C=C stretching vibration in alkenes
1479	-CH$_2$	Scissor vibration of CH$_2$
1387, 1380	C–H	Stretch vibration of C–H
1340	O–H	Phenolic O–H in-plane deformation
1317	P–O–C	Stretching mode of P–O–C groups on phosphate-carbon complexes
1200, 1117, 1115	C–O–C	C–O–C antisymmetric stretching vibration
1170, 1169	P=O	P=O stretching vibration in phosphorous oxyacids and phosphates
897, 894, 773	C–H	Out-of-plane deformation mode of C–H substituted in different benzene rings
692	C–H	C–H out-of-plane deformation of mono-substituted benzenes
460	C–O–C	C–O–C bend vibration in ethers

Fig. 5. Adsorption equilibrium isotherms at 25 °C on MFF_8 a) CO_2 and b) SF_6.

MFF_8 (best performing, pre-treated with phosphoric acid and post-treated for 12 days with propylene). Band assignments of Fig. 4 are summarized in Table 5.

Fig. 4 indicates that pre- and post-treatments, as well as carbonization end temperature, cause several changes in the surface chemistry of the samples. Namely, after carbonization most functional groups are removed, which is expected since several heteroatoms are released during this stage. However, in all samples O–H stretching vibrations ascribed to alcohols and phenols at 3400-3200 cm^{-1} and C–H stretching vibrations assigned to aliphatic compounds at 2950-2800 cm^{-1}, are present [64,65]. The bands located between 2364 and 2343 cm^{-1} are attributed to CO_2 present in the ambient air. Also, the O–H functional group intensity increases for sample MFF_2 pre-treated with phosphoric acid and decreases when post-treated with propylene, sample MFF_8. These results indicate that phosphoric acid should hydrolyze the surface of the carbon samples, as suggested by Myglovets et al. [66]. Not less important, in the CMS adsorbents a strong band at 1380 cm^{-1} assigned to C–H stretching vibration is observed [67]. Also, the sample pre-treated with phosphoric acid and not exposed to propylene, sample MFF_2, shows the presence of a C=O stretching vibration band at 1734 cm^{-1} [65]. Since the sample treated with propylene do not present this functional group, propylene should act as a cleaning agent of this oxygenated functional group, as reported before [47,48]. Spectra of samples pre-treated with phosphoric acid (Fig. 4b) and c)) indicate the presence of phosphor surface-functional groups, these samples exhibit a P=O stretching vibration band at 1170-1169 cm^{-1} [68–70]. However, the sample not exposed to propylene, MFF_2, displays a P–O–C stretching mode band at 1317 cm^{-1} assigned to P–O–C groups in phosphate-carbon complexes [69]. Since sample MFF_8, among the

three samples, is the one displaying the highest propane selectivity, the deletion of P–O–C and C=O functional groups and the presence of C=C and P=O groups in the adsorbent inner surface could also contribute for the observed performance.

3.6. Surface area and pore volume

Fig. 5 plots the carbon dioxide and sulfur hexafluoride adsorption equilibrium isotherms at 25 °C for sample MFF_8.

Fig. 5 indicates that MFF_8 CMS adsorbent displays a wide micropore size distribution since carbon dioxide (kinetic diameter of 0.33 nm [71]) and sulfur hexafluoride (kinetic diameter of 0.55 nm [72]) are highly adsorbed. Furthermore, the carbon dioxide amount adsorbed is clearly higher than the sulfur hexafluoride concentration, which reaches saturation at *ca.* 1.1 bar; the carbon dioxide isotherm reaches saturation above 7 bar. These results indicate a limited volume of pores larger than the size of sulfur hexafluoride.

Fig. 6 shows the CO_2 adsorption isotherm at 0 °C and the respective Dubinin-Astakhov linearization for MFF_8 CMS adsorbent. The DA

Table 6
Structural parameters for MFF_8 CMS sample.

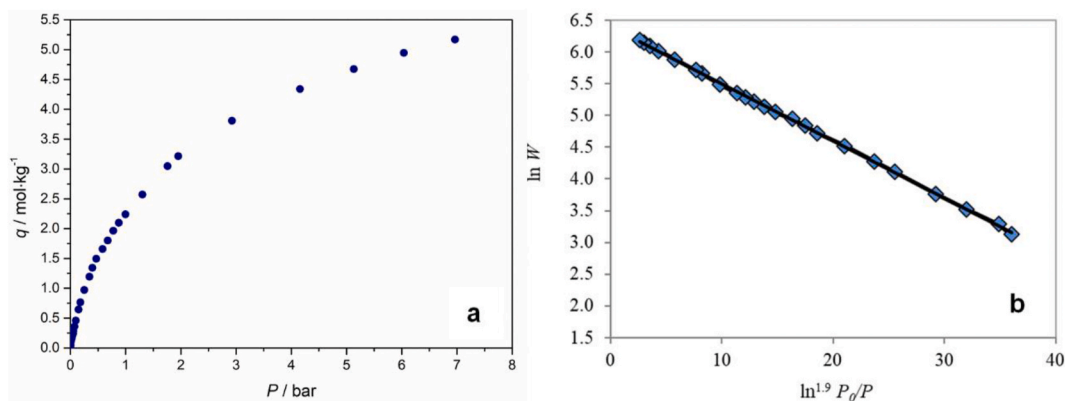| Parameter	MFF_8
n	1.9
$W_0/cm^3 \cdot kg^{-1}$	347.3
$E_0/kJ \cdot mol^{-1}$	9.4
$S/m^2 \cdot g^{-1}$	834.8

Fig. 6. CO_2 adsorption isotherm at 0 °C (a) and respective linearization employing Dubinin-Astakhov equation (b) for MFF_8 adsorbent (scatter corresponds to experimental data and solid line to DA fitting).
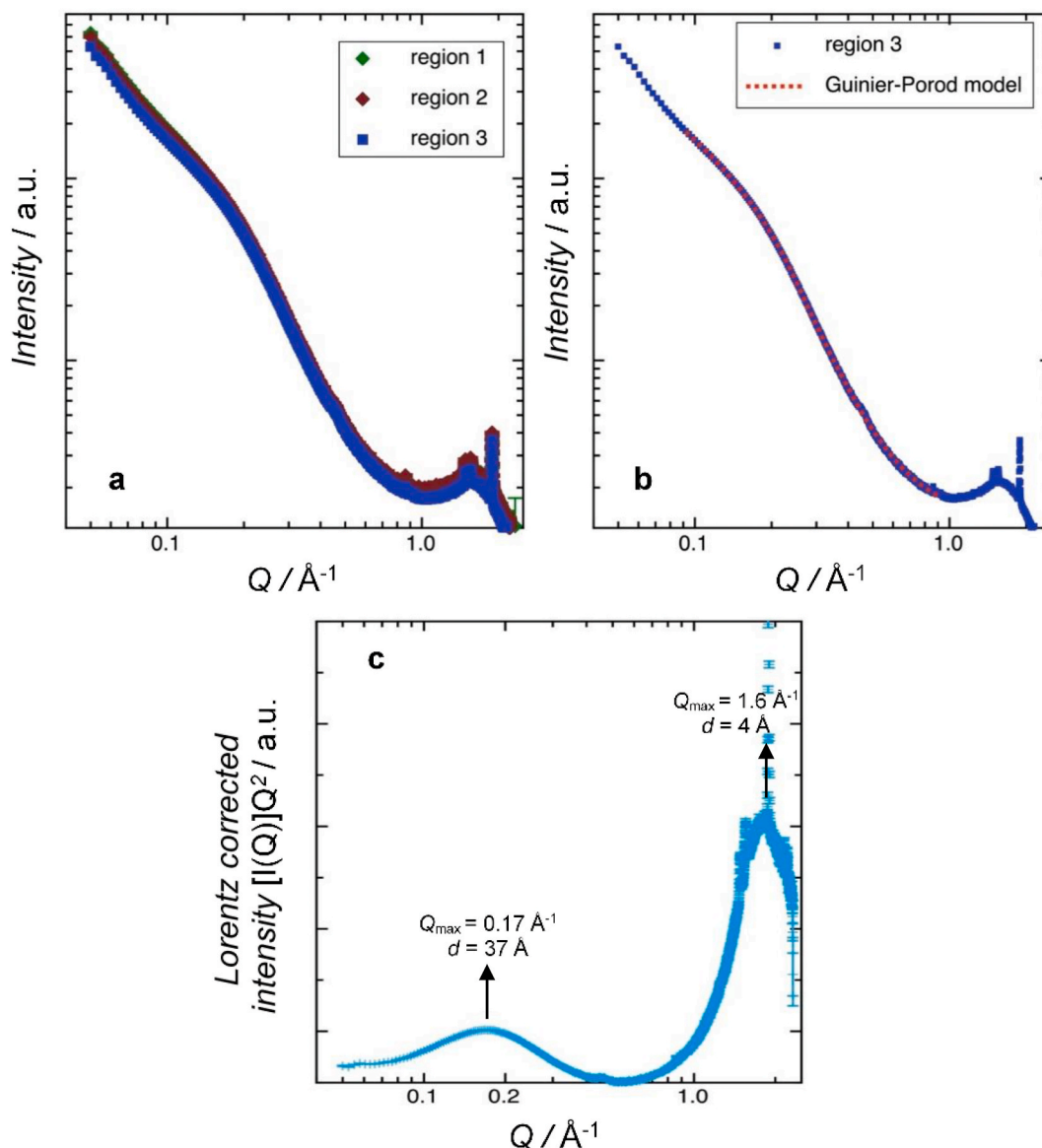
Fig. 7. SAXS data for MFF_8 for a) three spatially separated regions; b) data fitted to the Guinier-Porod model and c) Lorentz corrected SAXS data with a distribution of nanoscale structures centered around Q values of ca. 0.17 Å^{-1} and 1.6 Å^{-1} (a.u. = arbitrary units).

fitting parameters are given in Table 6.

The obtained specific surface area and micropore volume for MFF_8 adsorbent is in the range of other values reported in literature [73–77].

3.6.1. SAXS analysis

Small angle X-ray scattering (SAXS) was used for analysing the shape and size of MFF_8 CMS adsorbent pores [78]. The obtained results are shown in Fig. 7. SAXS data was fitted with the Guinier-Porod model [79] in the Q range from 0.1 Å^{-1} to 1.0 Å^{-1}. This model is empirical and can be used to determine the size and dimensionality of the nanopores including asymmetric nanopores with different shapes as spheres, rods, platelets as well as shapes intermediate between spheres and rods and between rods and platelets.

The Guinier-Porod model is given by equations (6) and (7):

$$I(Q) = \frac{G}{Q_s} \exp\left[\frac{-Q^2 R_g{}^2}{3-s}\right] \text{ for } Q \leq Q_1 \quad (6)$$

$$I(Q) = \frac{D}{Q_m} \text{ for } Q \geq Q_1 \quad (7)$$

where Q is the scattering variable, I is the scattered intensity, R_g is the radius of gyration and G and D are the Guinier and Porod scale factors, respectively. For globular pores (such as perfect spheres) $s = 0$, for rod shape (2D symmetry) structures $s = 1$ and for platelet shaped structures (1D symmetry) $s = 2$. The fitting parameters to the Guinier-Porod model (shown as red dots in Fig. 7b), are $s = 0.977$ and $R_g = 6.01$ Å. The value of s shows that the pores have approximately rod-shaped geometry. Considering that the radius-of-gyration of a randomly oriented cylinder of radius R is given by $R_g = R/\sqrt{2}$, then a value of $R \sim 8.5$ Å is obtained, i. e., the rods have then an average diameter of 1.7 nm.

The SAXS scattered intensity $I(Q)$, is related to the scattering vector amplitude, with the resultant $I(Q)$ coming from the subtraction of the appropriate background from the sample [80]. The momentum transfer value Q is related to the scattering angle and X-ray wavelength using the following:

$$Q = \frac{4\pi \sin \theta}{\lambda} \quad (8)$$

Bragg's law (Eq. (9)) can be applied for determining d, which is the lattice interplanar spacing of the crystal [78]:
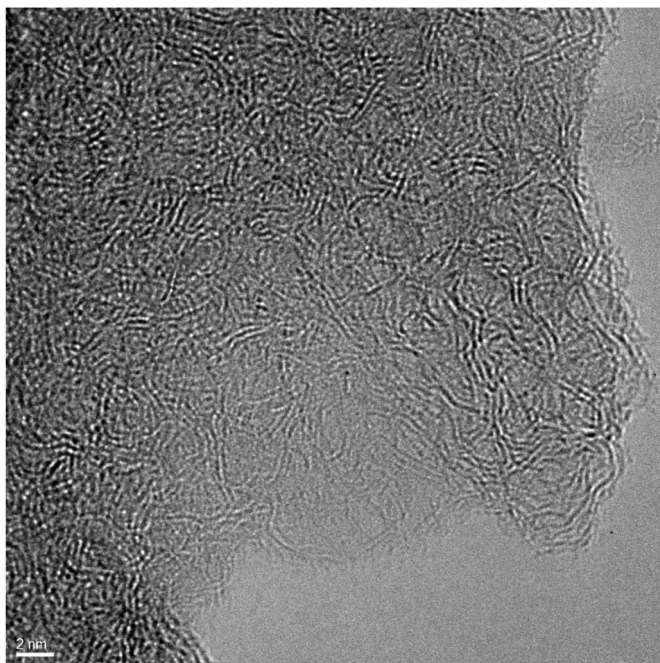
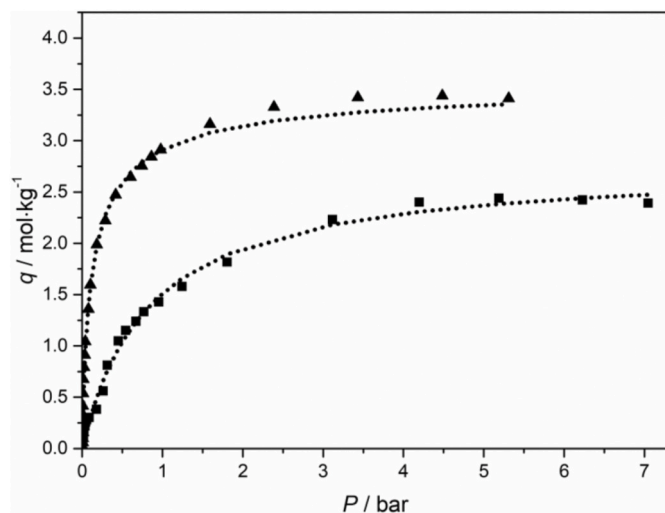**Fig. 8.** HRTEM image of a MFF carbon adsorbent carbonized at 1100 °C.

Table 7
Toth equation parameters of C_3H_6 and C_3H_8 on MFF_8 adsorbent.

Toth equation			
	q_s/mol·kg^{-1}	b/bar^{-1}	t
C_3H_6	2.89	1.30	0.89
C_3H_8	3.59	13.93	0.70

and pore size distribution.

3.6.2. Adsorption equilibrium and kinetics

The adsorption equilibrium isotherms of propane and propylene at 25 °C on sample MFF_8 are plotted in Fig. 9.

MFF_8 displays a higher adsorption capacity for propane compared with propylene; the adsorbed concentration ratio is *ca.* 2 at 1 bar. Normally, an activated carbon, as well as most of the adsorbents, are selective to propylene, which makes this adsorbent very special. This adsorbent is especially suited for the propylene purification, which implies the removal of small concentrations of propane. Table 7 shows the fitting parameters of the Toth equation for propane and propylene on MFF_8.

Fig. 10 shows the experimental uptake curves and the respective fitting model for propane and propylene at *ca.* 1 bar and 25 °C. The adsorption kinetics for both propane and propylene are very fast and similar, making this adsorbent suitable only for adsorption equilibrium separation processes. The separation mechanism that drives the separation is still unclear. However, the authors believe that the special morphology and size of the pores, as well as the presence of P=O groups and absence of C=O groups, may play a key role, preventing ingress of more rigid propylene molecules inside the adsorbent pore network.

4. Conclusions

Carbon molecular sieve adsorbents with kinetic and equilibrium selectivity to propane over propylene, were successfully prepared from a phenolic resin precursor. The phenolic resin precursor was pre-treated with phosphoric acid, followed by carbonization and propylene post-treatment. Ten samples were prepared changing the end temperature (950 °C – 1300 °C), pre-treatment (phosphoric acid concentration – 0 wt % to 25 wt%) and post-treatment (time of contact with propylene 0–12 days). The best performing samples, samples MFF_7 and MFF_8, were pre-treated with phosphoric acid at 25 wt%, carbonized at 1100 °C and post-treated with propylene for 6 and 12 days, respectively. MFF_7 exhibited a kinetic selectivity of propane over propylene of *ca.* 21 and MFF_8 displayed an equilibrium selectivity of *ca.* 2, at 1 bar and 25 °C. MFF_8 sample was fully characterized to investigate the reasons for this unprecedented equilibrium-based separation performance. The FTIR spectra showed that both, pre- and post-treatments, produce several changes in surface chemistry of the samples. Moreover, the results obtained from the volumetric method indicate that phosphoric acid may play a key role in the inverse equilibrium-based selectivity, since all samples pre-treated with phosphoric acid display a significant increase in the propane adsorption. On the other hand, the post-treatment with propylene, though relevant, has a smaller role for the equilibrium-based selectivity to propane. The propylene post-treatment opens the constrictions – more straight inter-pore connections, first increasing the diffusion kinetics to C_3H_8 – more flexible molecule – and then to C_3H_6, respectively. The SAXS analysis indicates that MFF_8 adsorbent has rod-shaped pores with a bimodal distribution and have an average pore size of 0.4 nm in the range of the ultra-micropores region. The HRTEM images show a earthworm network of micropores compatible with the SAXS analysis, both in terms of pore geometry and pore size distribution. The adsorption-based selectivity was assigned to the rod-shape ultra-microporosity, which should prevent the rigid propylene molecule to progress inside the adsorbent pore network. This conclusion opens the doors of carbon molecular sieve membranes to a completely different
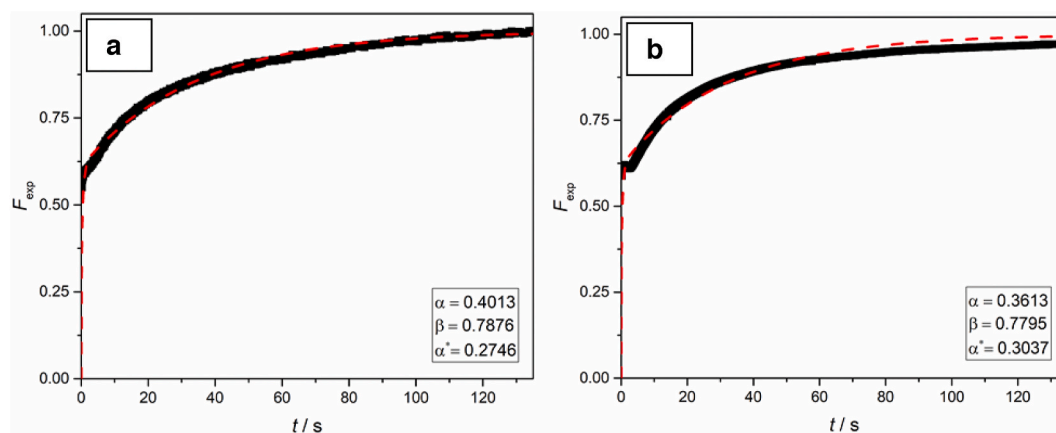

Fig. 9. Propane (▲) and propylene (■) experimental isotherms on MFF_8 at 25 °C. The dotted lines are the Toth equation fitting.

$$n\lambda = 2d \sin \theta \tag{9}$$

$$d = \frac{2\pi}{Q} \tag{10}$$

where θ is the X-ray incident angle (Bragg angle), n is an "integer", λ is the wavelength of the characteristic X-ray. Applying Eq. (10), the pore size distribution of the sample was determined for each Q_{max} value. Then, Fig. 7c) shows the pore size distribution of adsorbent MFF_8, which displays a bimodal size distribution with averages of 0.4 nm in the range of the ultra-micropores and 3.7 nm in the mesopore size range.

An HRTEM image was taken from a MFF carbon adsorbent carbonized at 1100 °C end temperature and 120 min of soaking time – Fig. 8. The carbon adsorbent was not submitted to any pre- or post-treatment.

Fig. 8 shows an earthworm network of micropores, compatible with the results obtained from SAXS analysis, both in terms of pore geometry

Fig. 10. Experimental uptake curves (black symbols) and fitting model (red dashed lines) for: a) propane and b) propylene. The fitting parameters are also given. (For interpretation of the references to colour in this figure legend, the reader is referred to the Web version of this article.)

class of gas separations, gas separations based on the molecular worming though rod-shape pores.

CRediT authorship contribution statement

Márcia Andrade: Investigation, Writing – original draft. **Andrew J. Parnell:** Investigation, (SAXS), Writing – review & editing. **Gabriel Bernardo:** Investigation, (SAXS), Writing – review & editing. **Adélio Mendes:** Supervision, Project administration, Funding acquisition, Writing – review & editing.

Declaration of competing interest

The authors declare that they have no known competing financial interests or personal relationships that could have appeared to influence the work reported in this paper.

References

[1] R.B. Eldridge, Olefin/paraffin separation technology: a review, Ind. Eng. Chem. Res. 32 (1993) 2208–2212.
[2] C.A. Grande, F. Poplow, A.E. Rodrigues, Vacuum pressure swing adsorption to produce polymer-grade propylene, Separ. Sci. Technol. 45 (2010) 1252–1259.
[3] P.F. Bryan, Removal of propylene from fuel-grade propane, Separ. Purif. Rev. 33 (2004) 157–182.
[4] A.M. Aitani, Propylene production. Encyclopedia of Chemical Processing, Taylor & Francis, New York, 2006, pp. 2461–2466.
[5] C. Gücüyener, J. van den Bergh, J. Gascon, F. Kapteijn, Ethane/ethene separation turned on its head: selective ethane adsorption on the Metal–Organic framework ZIF-7 through a gate-opening mechanism, J. Am. Chem. Soc. 132 (2010) 17704–17706.
[6] W. Zhu, F. Kapteijn, J.A. Moulijn, Shape selectivity in the adsorption of propane/propene on the all-silica DD3R, Chem. Commun. (1999) 2453–2454.
[7] S.C. Reys, V.V. Krishnan, G.J. DeMartin, J.H. Sinfelt, K.G. Strohmaier, S. Jg, Separation of propylene from hydrocarbon mixtures, USOO6730142B2 (2004).

[8] M.C. Campo, A.M. Ribeiro, A. Ferreira, J.C. Santos, C. Lutz, J.M. Loureiro, A. E. Rodrigues, New 13X zeolite for propylene/propane separation by vacuum swing adsorption, Separ. Purif. Technol. 103 (2013) 60–70.
[9] M. Mofarahi, M. Sadrameli, J. Towfighi, Four-bed vacuum pressure swing adsorption process for propylene/propane separation, Ind. Eng. Chem. Res. 44 (2005) 1557–1564.
[10] J.W. Chang, T.R. Marrero, H.K. Yasuda, Continuous process for propylene/propane separation by use of silver nitrate carrier and zirconia porous membrane, J. Membr. Sci. 205 (2002) 91–102.
[11] I.G. Giannakopoulos, V. Nikolakis, Recovery of hydrocarbons from mixtures containing C3H6, C3H8 and N2 using NaX membranes, J. Membr. Sci. 305 (2007) 332–337.
[12] X. Ma, S. Williams, X. Wei, J. Kniep, Y.S. Lin, Propylene/propane mixture separation characteristics and stability of carbon molecular sieve membranes, Ind. Eng. Chem. Res. 54 (2015) 9824–9831.
[13] N. Schmeling, R. Konietzny, D. Sieffert, P. Rolling, C. Staudt, Functionalized copolyimide membranes for the separation of gaseous and liquid mixtures, Beilstein J. Org. Chem. 6 (2010) 789–800.
[14] G.Q. Zhu, C.G. Xie, Research and commercial application of CPP technology for producing light olefins from heavy oil, China Pet. Process. Petrochem. Technol. 15 (2013) 7–12.
[15] T. Ren, M. Patel, K. Blok, Olefins from conventional and heavy feedstocks: energy use in steam cracking and alternative processes, Energy 31 (2006) 425–451.
[16] K. Fukudome, T. Suzuki, Highly selective oxidative dehydrogenation of propane to propylene over VOx–SiO2 catalysts, Catal. Surv. Asia 19 (2015) 172–187.
[17] T.K. Ghosh, H.D. Lin, A.L. Hines, Hybrid adsorption-distillation process for separating propane and propylene, Ind. Eng. Chem. Res. 32 (1993) 2390–2399.
[18] J. Park, K. Kim, J.-W. Shin, K. Tak, Y.-K. Park, Performance study of multistage membrane and hybrid distillation processes for propylene/propane separation, Can. J. Chem. Eng. 95 (2017) 2390–2397.
[19] V. Sakhre, Reactive distillation: modeling, simulation, and optimization, in: V. Steffen (Ed.), Distillation - Modelling, Simulation and Optimization, Intech Open, 2019.
[20] S.U. Rege, J. Padin, R.T. Yang, Olefin/paraffin separations by adsorption: pi-complexation vs. kinetic separation, AIChE J. 44 (1998) 799–809.
[21] R.W. Baker, Future directions of membrane gas separation technology, Ind. Eng. Chem. Res. 41 (2002) 1393–1411.
[22] J. Padin, S.U. Rege, R.T. Yang, L.S. Cheng, Molecular sieve sorbents for kinetic separation of propane/propylene, Chem. Eng. Sci. 55 (2000) 4525–4535.
[23] J.-J. Kim, S.-J. Lim, H. Ahn, C.-H. Lee, Adsorption equilibria and kinetics of propane and propylene on zeolite 13X pellets, Microporous Mesoporous Mater. 274 (2019) 286–298.
[24] H. Abdi, H. Maghsoudi, All-silica DD3R zeolite for adsorptive separation of propylene from propane: equilibrium and kinetic data, Microporous Mesoporous Mater. 307 (2020) 110513.
[25] Q. Dong, Z. Song, F. Zhou, H. Li, M. Yu, Ultrathin, fine-tuned microporous coating modified 5A zeolite for propane/propylene adsorptive separation, Microporous Mesoporous Mater. 281 (2019) 9–14.
[26] J.G. Min, K.C. Kemp, S.B. Hong, Propylene/propane separation on a ferroaluminosilicate levyne zeolite, Microporous Mesoporous Mater. 294 (2020) 109833.
[27] S. Shrestha, P.K. Dutta, Modification of a continuous zeolite membrane grown within porous polyethersulfone with Ag(I) cations for enhanced propylene/propane gas separation, Microporous Mesoporous Mater. 279 (2019) 178–185.
[28] D. Saha, B. Toof, R. Krishna, G. Orkoulas, P. Gismondi, R. Thorpe, M.L. Comroe, Separation of ethane-ethylene and propane-propylene by Ag(I) doped and sulfurized microporous carbon, Microporous Mesoporous Mater. 299 (2020) 110099.
[29] C. Herdes, A. Valente, Z. Lin, J. Rocha, J.A.P. Coutinho, F. Medina, L.F. Vega, Selective adsorption of volatile organic compounds in micropore aluminum

methylphosphonate-α: A combined molecular Simulation−Experimental approach, Langmuir 23 (2007) 7299–7305.

[30] K. Maeda, J. Akimoto, Y. Kiyozumi, F. Mizukami, Structure of aluminium methylphosphonate, AlMePO-β, with unidimensional channels formed from ladder-like organic–inorganic polymer chains, Journal of the Chemical Society, Chem. Commun. (1995) 1033–1034.

[31] M. Edgar, V.J. Carter, D.P. Tunstall, P. Grewal, V. Favre-Nicolin, P.A. Cox, P. Lightfoot, P.A. Wright, Structure solution of a novel aluminium methylphosphonate using a new simulated annealing program and powder X-ray diffraction data, Chemical Communications (2002) 808–809.

[32] S.P. Brown, S.E. Ashbrook, S. Wimperis, ^{27}Al multiple-quantum magic angle spinning NMR study of the thermal transformation between the microporous aluminum methylphosphonates AlMePO-β and AlMePO-α, J. Phys. Chem. B 103 (1999) 812–817.

[33] N. Li, S. Xiang, Hydrothermal synthesis and crystal structure of two novel aluminophosphites containing infinite Al–O–Al chains, J. Mater. Chem. 12 (2002) 1397–1400.

[34] K. Maeda, Metal phosphonate open-framework materials, Microporous Mesoporous Mater. 73 (2004) 47–55.

[35] K. Maeda, Y. Kiyozumi, F. Mizukami, Characterization, Gas Adsorption Properties, Of aluminum methylphosphonates with organically lined unidimensional channels, J. Phys. Chem. B 101 (1997) 4402–4412.

[36] M.C. Kroon, L.F. Vega, Selective paraffin removal from ethane/ethylene mixtures by adsorption into aluminum methylphosphonate-α: a molecular simulation study,, Langmuir 25 (2009) 2148–2152.

[37] C. Serre, A. Vimont, P. Llewellyn, J.-S. Chang, P. Horcajada, e.a. Ferey G, Reducible porous crystalline hybrid solid for the separation of mixtures of molecules having different degrees and/or a different number of unsaturations, WO 2010/000975 A1 (2010).

[38] J. van den Bergh, C. Gücüyener, E.A. Pidko, E.J.M. Hensen, J. Gascon, F. Kapteijn, Understanding the anomalous alkane selectivity of ZIF-7 in the separation of light alkane/alkene mixtures, Chem. Eur. J. 17 (2011) 8832–8840.

[39] E. Andres-Garcia, L. Oar-Arteta, J. Gascon, F. Kapteijn, ZIF-67 as silver-bullet in adsorptive propane/propylene separation, Chem. Eng. J. 360 (2019) 10–14.

[40] U. Böhme, B. Barth, C. Paula, A. Kuhnt, W. Schwieger, A. Mundstock, J. Caro, M. Hartmann, Ethene/ethane and propene/propane separation via the olefin and paraffin selective metal–organic framework adsorbents CPO-27 and ZIF-8, Langmuir 29 (2013) 8592–8600.

[41] F.A.D. Silva, A.E. Rodrigues, Propylene/propane separation by vacuum swing adsorption using 13X zeolite, AIChE J. 47 (2001) 341–357.

[42] C.A. Grande, J. Gascon, F. Kapteijn, A.E. Rodrigues, Propane/propylene separation with Li-exchanged zeolite 13X, Chem. Eng. J. 160 (2010) 207–214.

[43] D.H. Olson, M.A. Camblor, L.A. Villaescusa, G.H. Kuehl, Light hydrocarbon sorption properties of pure silica Si-CHA and ITQ-3 and high silica ZSM-58, Microporous Mesoporous Mater. 67 (2004) 27–33.

[44] D.D. Do, H.D. Do, Cooperative, Competitive Adsorption, Of ethylene, ethane, nitrogen and argon on graphitized carbon black and in slit pores, Adsorption 11 (2005) 35–50.

[45] F.J. Keil, Molecular Simulation of Adsorption in Zeolites and Carbon Nanotubes, in: L.J. Dunne, G. Manos (Eds.), Adsorption and Phase Behaviour in Nanochannels and Nanotubes, Springer Netherlands, Dordrecht, 2010, pp. 9–40.

[46] S. Jakobtorweihen *, N. Hansen, F.J. Keil, Molecular simulation of alkene adsorption in zeolites, Mol. Phys. 103 (2005) 471–489.

[47] C.W. Jones, W.J. Koros, Carbon molecular sieve gas separation membranes-II. Regeneration following organic exposure, Carbon 32 (1994) 1427–1432.

[48] S.C. Rodrigues, M. Andrade, J. Moffat, F.D. Magalhães, A. Mendes, Carbon membranes with extremely high separation factors and stability, Energy Technol. 7 (2019) 1801089.

[49] I. Menendez, A.B. Fuertes, Aging of carbon membranes under different environments, Carbon 39 (2001) 733–740.

[50] T. Budinova, E. Ekinci, F. Yardim, A. Grimm, E. Björnbom, V. Minkova, M. Goranova, Characterization and application of activated carbon produced by H3PO4 and water vapor activation, Fuel Process. Technol. 87 (2006) 899–905.

[51] M. Ottaway, Use of thermogravimetry for proximate analysis of coals and cokes, Fuel 61 (1982) 713–716.

[52] C. Nguyen, D.D. Do, K. Haraya, K. Wang, The structural characterization of carbon molecular sieve membrane (CMSM) via gas adsorption,, J. Membr. Sci. 220 (2003) 177–182.

[53] C. Nguyen, D.D. Do, Adsorption of supercritical gases in porous Media: determination of micropore size distribution, J. Phys. Chem. B 103 (1999) 6900–6908.

[54] M.M.C.C. Santos, Carbon molecular sieve membranes for gas separation: study, preparation and characterization, Porto2009.

[55] S.C. Rodrigues, R. Whitley, A. Mendes, Preparation and characterization of carbon molecular sieve membranes based on resorcinol–formaldehyde resin, J. Membr. Sci. 459 (2014) 207–216.

[56] D.D. Do, Adsorption analysis: equilibria and kinetics, Queensland (1998).

[57] SasView for small angle scattering analysis. https://www.sasview.org/, 2020.

[58] D. Ferreira, R. Magalhães, P. Taveira, A. Mendes, Effective adsorption equilibrium isotherms and breakthroughs of water vapor and carbon dioxide on different adsorbents, Ind. Eng. Chem. Res. 50 (2011) 10201–10210.

[59] J.C. Santos, F.D. Magalhães, A. Mendes, Contamination of zeolites used in oxygen production by PSA: effects of water and carbon dioxide, Ind. Eng. Chem. Res. 47 (2008) 6197–6203.

[60] M. Kočiřík, P. Struve, M. Bülow, Analytical solution of simultaneous mass and heat transfer in zeolite crystals under constant-volume/variable-pressure conditions, Journal of the Chemical Society, Faraday Transactions 1: Physical Chemistry in Condensed Phases 80 (1984) 2167–2174.

[61] E.V. Krivokorytov, A.G. Gur'ev, B.I. Polyak, High-carbon binders in refractories and corrosion-resistant ceramics technology, Glass Ceram. 55 (1998) 144–147.

[62] R. Lum, C.W. Wilkins, M. Robbins, A.M. Lyons, R.P. Jones, Thermal analysis of graphite and carbon-phenolic composites by pyrolysis-mass spectrometry, Carbon 21 (1983) 111–116.

[63] P. Xu, X. Jing, High carbon yield thermoset resin based on phenolic resin, hyperbranched polyborate, and paraformaldehyde, Polym. Adv. Technol. 22 (2011) 2592–2595.

[64] M.A. Mohamed, J. Jaafar, A.F. Ismail, M.H.D. Othman, M.A. Rahman, Chapter 1-Fourier Transform Infrared (FTIR) Spectroscopy, in: N. Hilal, A.F. Ismail, T. Matsuura, D. Oatley-Radcliffe (Eds.) Membrane Characterization, Elsevier2017, pp. 3–29.

[65] Z.Q. Chen, Y.F. Chen, H.B. Liu, Pyrolysis of phenolic resin by TG-MS and FTIR analysis, Adv. Mater. Res. 631–632 (2013) 104–109.

[66] M. Myglovets, O.I. Poddubnaya, O. Sevastyanova, M.E. Lindström, B. Gawdzik, M. Sobiesiak, M.M. Tsyba, V.I. Sapsay, D.O. Klymchuk, A.M. Puziy, Preparation of carbon adsorbents from lignosulfonate by phosphoric acid activation for the adsorption of metal ions, Carbon 80 (2014) 771–783.

[67] O.A. Ekpete, A.C. Marcus, V. Osi, Preparation and characterization of activated carbon obtained from plantain (musa paradisiaca) fruit stem, J. Chem. 2017 (2017) 8635615.

[68] A.M. Puziy, O.I. Poddubnaya, A. Martínez-Alonso, F. Suárez-García, J.M.D. Tascón, Synthetic carbons activated with phosphoric acid: I. Surface chemistry and ion binding properties, Carbon 40 (2002) 1493–1505.

[69] S. Bourbigot, M. Le Bras, R. Delobel, P. Bréant, J.-m. Trémillon, Carbonization mechanisms resulting from intumescence-part II. Association with an ethylene terpolymer and the ammonium polyphosphate-pentaerythritol fire retardant system, Carbon 33 (1995) 283–294.

[70] S.M. Yakout, G. Sharaf El-Deen, Characterization of activated carbon prepared by phosphoric acid activation of olive stones, Arabian Journal of Chemistry 9 (2016) S1155–S1162.

[71] N. Mehio, S. Dai, D.-e. Jiang, quantum mechanical basis for kinetic diameters of small gaseous molecules, J. Phys. Chem. 118 (2014) 1150–1154.

[72] T. Hasell, M. Miklitz, A. Stephenson, M.A. Little, S.Y. Chong, R. Clowes, L. Chen, D. Holden, G.A. Tribello, K.E. Jelfs, A.I. Cooper, Porous organic cages for sulfur hexafluoride separation, J. Am. Chem. Soc. 138 (2016) 1653–1659.

[73] S.R. Tennison, Phenolic-resin-derived activated carbons, Applied Catalysis A: Gene (Amst.) 173 (1998) 289–311.

[74] C. Lei, N. Amini, F. Markoulidis, P. Wilson, S. Tennison, C. Lekakou, Activated carbon from phenolic resin with controlled mesoporosity for an electric double-layer capacitor (EDLC), J. Mater. Chem. 1 (2013) 6037–6042.

[75] D. Lee, J.Y. Jung, M.S. Park, Y.S. Lee, Preparation of novolac-type phenol-based activated carbon with a hierarchical pore structure and its electric double-layer capacitor performance, Carbon Letters 15 (2014) 192–197.

[76] K. Nakagawa, S.R. Mukai, K. Tamura, H. Tamon, Mesoporous activated carbons from phenolic resins, Chem. Eng. Res. Des. 85 (2007) 1331–1337.

[77] Y. Li, Z.h. Huang, F.y. Kang, B.h. Li, Preparation of activated carbon microspheres from phenolic resin with metal compounds by sub- and supercritical water activation, N. Carbon Mater. 25 (2010) 109–113.

[78] A.K. Singh, Chapter 4-Experimental Methodologies for the Characterization of Nanoparticles, in: A.K. Singh (Ed.), Engineered Nanoparticles, Academic Press, Boston, 2016, pp. 125–170.

[79] B. Hammouda, A new Guinier-Porod model,, J. Appl. Crystallogr. 43 (2010) 716–719.

[80] L. Boldon, F. Laliberte, L. Liu, Review of the fundamental theories behind small angle X-ray scattering, molecular dynamics simulations, and relevant integrated application, Nano Rev. 6 (2015) 25661.